Structural integrity of polymers processed by additive manufacturing techniques using residual strength diagrams

A.J. Cano [a], A. Salazar [a,b,*], J. Rodríguez [a,b]

[a] DIMME, Grupo de Durabilidad e Integridad Mecánica de Materiales Estructurales, Universidad Rey Juan Carlos. C/ Tulipán, s/n. 28933 Móstoles, Madrid, Spain
[b] Instituto de Investigación de Tecnologías para la Sostenibilidad, Universidad Rey Juan Carlos. C/ Tulipán, s/n. 28933 Móstoles, Madrid, Spain

ARTICLE INFO

ABSTRACT

Motivated by the increasingly important role that polymers have in structural applications, this study aims to analyse the structural integrity of polymers through residual strength diagrams. The polymers analysed have been thermoplastics, Polylactic acid (PLA), Polyethylene terephthalate glycol-modified (PET-G) and Polyamide 12 (PA-12), as well as a thermosetting resin, processed through different additive manufacturing techniques: Fused Deposition Modelling (FDM) in the case of PLA, PET-G, Selective Laser Sintering (SLS) for PA-12 and Digital Light Processing (DLP) for the thermosetting resin. In addition, PA-12 manufactured by injection moulding was also included in this study. To obtain the residual strength diagrams, mechanical tests have been carried out on smooth specimens and on specimens with cracks of different lengths. From the analysis of the results, a prediction has been obtained by fitting a semi-empirical model that describes the structural integrity in the areas of microstructurally short cracks, long cracks and physically short cracks.

1. Introduction

The fact that cracks or flaws in a material reduce its strength below that described by the strength of the material has been known for decades. This led to the introduction of residual strength as a critical design parameter in the safe-life design of engineered components and the beginning of damage tolerance programmes in engineering [1,2]. Thus, damage tolerance is the working philosophy of Fracture Mechanics, a discipline that was born to address the residual strength of cracked components. Initially designed to be applied to solids with cracks of any size, in the 1960 s it was found not to be applicable to microstructurally short cracks [3], as these do not comply with the laws of Continuum Mechanics [4], nor to physically short cracks, defined in metals as those whose size is comparable to the plastic deformation zone generated at the crack tip where the Linear Elastic Fracture Mechanics approach (LEFM) is not applicable, i.e. smaller than 1 or 2 mm [4].

The problem of physically short cracks is a pressing and current problem in the analysis of mechanical behaviour since its behaviour cannot be described with criteria based on the field of stresses or deformations or with the approximation of Fracture Mechanics [4,5].

The residual strength diagrams can be considered modifications of the Kitagawa-Takahashi diagram in which fatigue failure occurs for 1/2 cycle [6–9]. In this case, the maximum strength, versus the size of the defect is represented and constructed from the mechanical strength obtained from smooth specimens, σ_T, and the fracture toughness, K_{IC}, obtained from cracked specimens (Fig. 1). It is possible to combine these two parameters in the characteristic length, l_0, which can be interpreted as the defect length below which the mechanical strength of the material is not modified.

$$l_0 = \frac{1}{\pi} \left(\frac{K_{IC}}{\sigma_T} \right)^2 \tag{1}$$

To address the problem of physically short cracks, El Haddad proposed replacing the Kitagawa-Takahashi diagram with an empirical equation,

$$\frac{\sigma}{\sigma_T} = \sqrt{\frac{l_0}{a + l_0}} \tag{2}$$

being σ the strength of a solid with a crack length, a. The residual diagram so obtained can be divided into three zones: ① region in which the size of the defects is microstructurally short and, therefore, the mechanical strength is not affected; ③ the region of long cracks described by Fracture Mechanics; and ② a transition zone, in which the behaviour

---

* Corresponding author at: DIMME, Grupo de Durabilidad e Integridad Mecánica de Materiales Estructurales, Universidad Rey Juan Carlos. C/ Tulipán, s/n. 28933 Móstoles, Madrid, Spain.
E-mail address: alicia.salazar@urjc.es (A. Salazar).

| Nomenclature			
			model
		LEFM	Linear Elastic Fracture Mechanics
a	Crack length	PA-12	Polyamide 12
a_0	Initial crack length	PET-G	Polyethylene terephthalate glycol-modified
B	Specimen thickness	PLA	Polylactic acid
DLP	Digital Light Processing	PMMA	Poly(methyl methacrylate)
$\overline{D}$	Spherulite diameter	R_a	Average roughness through the profile
f	Geometric factor	R_z	Average of the maximum peak to valley distances
E	Young Modulus	SLS	Selective Laser Sintering
FDM	Fused Deposition Modelling	U	Area under the load-displacement curve
IM	Injection moulding	W	Specimen width
J_{IC}	J-integral at crack growth initiation	ε	Engineering strain
K_C^*	Estimated Fracture Toughness from the theory of critical distances	ε_R	Elongation at break
		ε_u	Elongation at maximum stress
K_{IC}	Fracture toughness	η	Geometric factor
K_J	Stress intensity factor obtained from J-integral	ν	Poisson's ratio
l_{ch}	Cohesive zone length	σ	Engineering stress
l_0	Characteristic length in El Haddad empirical model	σ_T	Maximum tensile strength
l_0^{crazes}	Craze zone length from Dugdale-Barenblatt strip-yield	χ_c	Cristallinity degree
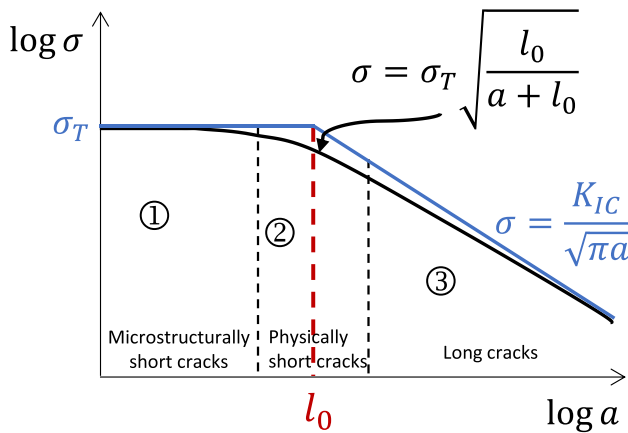
Fig. 1. Residual strength diagram.

is nonlinear, and follows equation (2), analogous to that used to describe the fatigue behaviour by El Haddad [7–9].

It is important to make clear that this approach is purely phenomenological and describes the behavior of cracked solids based on only two parameters: K_{IC} and σ_T. The combination of these parameters also gives rise to characteristic lengths in other theoretical approaches, such as cohesive zone models where the length l_{ch} is introduced:

$$l_{ch} = \frac{K_{IC}^2}{\sigma_T^2} \quad (3)$$

This characteristic length l_{ch} can be interpreted as the size of the cohesive zone that is generated ahead of the tip of a long crack. It is a measure of the brittleness of the material, the smaller the l_{ch}, the more brittle the material is. The advantage of cohesive models is that they can be applied to linear or nonlinear fractures, such as those developed in polymers by crazing or shear yielding [10].

Additionally, the characteristic length l_0 is called critical distance in the theory of the critical distances. Moreover, an identical expression to that of equation (1) is also derived to determine the fracture stress in notched samples linking the imaginary crack method to the point method and the line method [11], although the meaning of σ_T in the analysis of failure of notched specimens may require reinterpretation [12,13].

The relationship between l_0 and microstructural characteristics is not always possible. Sometimes very direct correlations have been found with microstructural variables such as grain size, other times relationships have been sought with the distance from the surface of the specimen to microstructural barriers that serve as an obstacle to the advancement of cracks. In some polymeric materials the value of l_0 has been linked to the size of a craze. However, it must be recognized that on many other occasions it has not been possible to link it with microstructural features and, therefore, it must be interpreted as a measure of the fracture process zone, whose value allows discriminating by its size the relevant defects in the residual strength of a solid [14].

Residual strength diagrams for metals have been used in numerous works, Feddersen started implementing them on aluminium alloys of the 2s and 7s series, representing them with a double linear scale. He achieved good predictability of the behaviour in both series [2]. Wu et al. represented the tests carried out on CS1030 steel pipes and also obtained a good fit between the experimental data and the model prediction [15]. Apart from metallic alloys, more recent studies such as the one carried out by Sutrakar et al. apply the same methodology to the simulation of residual strength in graphene, but the results still need to be checked against experimental data [16]. Although there is no doubt that polymers are acquiring an increasingly relevant role in structural applications in different technological sectors, intensified even more with the implementation of additive manufacturing techniques, residual strength diagrams for these materials are still scarce. Berry obtained these diagrams for Polystyrene and for Polymethylmethacrylate, resulting in a prediction very well adjusted to the experimental data obtained and, comparatively, a higher residual strength for Polystyrene [17]. Despite the good fit and prediction given by these diagrams, to date they have not been published for any polymer manufactured by additive manufacturing techniques as far as the authoŕs knowledge.

Therefore, the aim of this work is to evaluate the structural integrity by residual strength diagrams of thermoplastic and thermoset polymeric materials processed by additive manufacturing techniques.

2. Experimental procedure

2.1. Materials

The materials under study have been a commercial photocurable thermosetting resin, and 3 thermoplastic polymers: polylactic acid (PLA), polyethylene terephthalate glycol-modified (PET-G) and polyamide 12 (PA-12) [18].
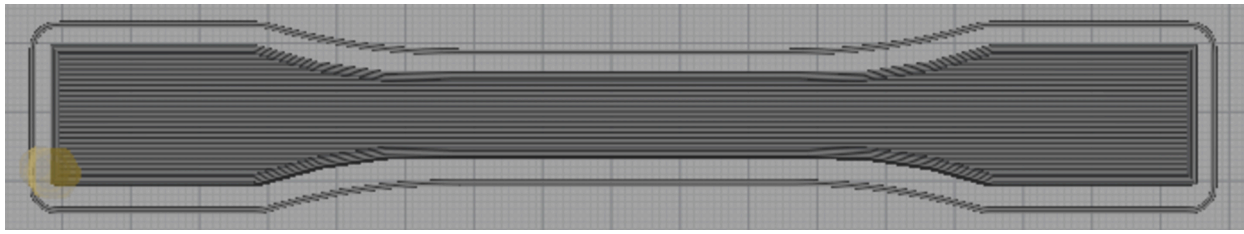
Fig. 2. Direction of deposition used in FDM manufacture of PLA and PET-G.

The thermosetting resin used has the trade name Monocure 3D Rapid® and it is composed of a hexamethylene diacrylate base (>60 % by weight), (1-methyl-1,2-ethanediyl)bis[oxy(methyl-2,1-ethanediyl) diacrylate (<20 % by weight) and photoinitiators. It has been processed by the Digital Light Processing (DLP) technique with a Creality LD-006 set up, using a curing time of 6 s per layer, a layer height of 50 μm and a 2-step post-processing: cleaning with isopropanol and 3 min post-curing with UV light. For setting these processing parameters a previous optimization process to obtain the highest dimensional accuracy and mechanical strength was carried out taking as starting point the manufacturer's recommendations.

In the case of PLA and PET-G, the Fused Deposition Modelling (FDM) technique has been employed. The equipment utilised was the BCN3D Sigma R19. For the setup of the processing parameters also a previous optimisation process was performed taking as benchmark the values of the parameters obtained from the literature [19] to attain full dense and high mechanical performance properties. The common processing parameters for PLA and PET-G were the layer height of 0.2 mm, the infill density of 100%, and the print speed of 45 mm/min. In the case of PLA, the extrusion temperature was 205 °C, while that of the printing bed was 50 °C. In PET-G, these temperatures were 240 °C and 90 °C, respectively. In both cases, the filament was deposited in a parallel orientation to the direction of load application, specifically at 0° (Fig. 2), which represents the optimal configuration, as evidenced by various literature sources [19].

Finally, for the processing of the PA-12, the additive manufacturing technique of Selective Laser Sintering (SLS) has been used and the study has been also carried out in samples processed by the conventional technique of Injection Moulding (IM). SLS PA-12 was manufactured by Prodintec, S.L., Spain and IM PA-12 by Aires Industrias del Plástico, S.A., Spain. For the PA-12 specimens processed by SLS, an EOS Formiga P-100 LS equipment with CO_2 laser with a power of 25 W was used using the PA2200 of the EOS family as a starting powder. During processing, the temperatures of the chamber and of the powder bed were 135.5 °C and 171.5 °C, respectively. The specimens were manufactured with a layer thickness of 0.2 mm with two different orientations, one of them contained in the melting plane, 0°, and the other perpendicular to it, 90°. In the case of specimens manufactured by IM, the starting material was PA-12 Evonik Vestamid in pellet form. The mold temperature was 60 °C and the material was injected with a speed of 6–8 mm/s, with a pressure of 10 MPa and with a filling time of 2.1 s. A clamping force of 1500 kN was applied to the mold for 6.5 s.

Regarding the physical properties and the microstructural features of the materials under study, the thermosetting resin, PETG, PLA and IM PA-12 are fully dense materials (porosity percentage of less than 1 %) while both SLS PA-12 showed a porosity percentage of 3.7 ± 0.5 %. The size of the pores in SLS PA-12 was measurable by inspection through Scanning Electron Microscopy, obtaining values of the order of the size of the sintering powder, 90 ± 50 μm, since the pores were caused by the unmolten particles. The crystallinity degree, χ_c, and the diameter of the crystalline phase or spherulites, $\overline{D}$, were microstructural characteristics of PA-12, with the particularity that the IM PA-12 presented a skin-core morphology where the spherulites were only measurable in the core region while in the skin only the amorphous phase prevailed. This

Table 1

Microstructural and mesoscopic features of the materials under study semi-crystalline polymers as SLS PA-12 and IM PA-12. The crystallinity degree, χ_c, the diameter of the crystalline phase or spherulites, $\overline{D}$, as microscopic features and size of the pores, when discernible, the layer height and the skin depth as mesoscopic characteristics are included [20–22].

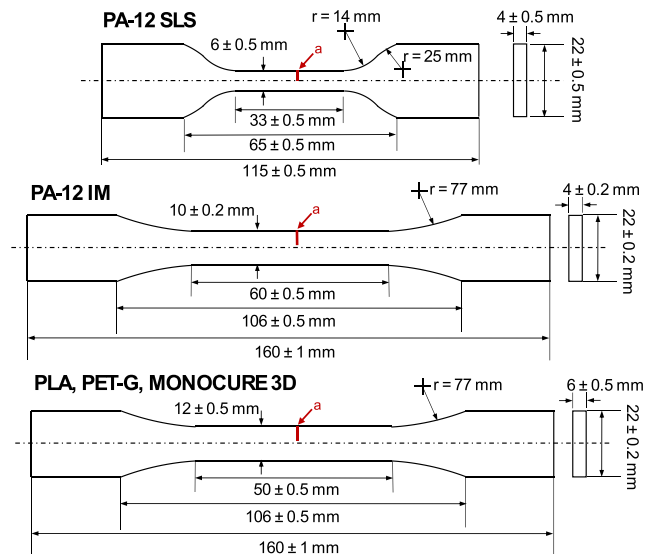| Material	Microscopic features		Mesoscopic features		
	χ_c (%)	$\overline{D}$(μm)	Pore size (μm)	Layer height (μm)	Skin depth (μm)
Monocure 3D	–	–	–	50	
PLA	–	–	–	200	
PET-G	–	–	–	200	
SLS PA-12	33 ± 2	48 ± 12	90 ± 50	200	–
IM PA-12	37.0 ± 0.2	13 ± 3	–		250 ± 50

Fig. 3. Dimensions and geometry of the used dumbbell specimens made of PA-12 manufactured by SLS and IM and of PLA, PET-G and MONOCURE 3D resin. The red line represents the location of the crack, a, in the cracked specimens.

morphology was usually generated in injection moulding processes where the high injection speed and the rapid cooling impede the crystallisation in the skin. It is important to mention that no differences were appreciable in the crystalline degree and the spherulite size between SLS PA12 0° and 90°. The most relevant microstructural features are collected in Table 1 and more details about the measured properties can be found in [20–22]. Moreover, in some samples, a mesoscopic structure related to the processing parameters is also discernible in the microstructural analysis, this was the layer height in specimens processed by SLS, FDM and DLP and has been also included in Table 1.

2.2. Mechanical characterization

To estimate the size of the surface defects in plain specimens, the surface roughness has been measured using a Mitutoyo SJ-301 contact roughness with a detector with a tip radius of 60 μm and a tip angle of 60°. To this end, the mean value of six measurements in the longitudinal direction and six in the transverse direction, relative to the axis of the dumbbell specimen, was determined for each material.

The mechanical characterization was carried out at 21 °C following the guidelines of ASTM D638-14, Standard Method for Tensile Properties of Plastics [23], using dumbbell tensile test samples, with dimensions of the gage zone of 50x12x6 mm^3 for thermoset resin, PLA and PET-G, 33x6x4 mm^3 for SLS PA-12 and 60x10x4 mm^3 for IM PA-12 [21,22] (Fig. 3). Tests were conducted on both smooth and cracked specimens using an MTS Alliance RF/100 universal electromechanical testing machine equipped with a load cell of ± 5 kN, at a constant cross-head speed of 5 mm/min yielding a strain rate of 2.5·10^{-3} s^{-1} in SLS PA-12, 1.4·10^{-3} s^{-1} in IM PA-12 and 1.7·10-3 s^{-1} in PLA, PET-G and Monocure 3D. A contact extensometer MTS 634.12F-54 for axial elongation measurements was employed instead of the cross-head displacement of the electromechanical machine for all the materials except for the IM PA-12 in which cross-head displacement had to be used due to the stretchability of the material.

The introduction of cracks was conducted in the central region of the specimen, as illustrated in Fig. 3. The employed techniques were designed to minimise damage, considering the prior expertise of the authors with other thermoplastic polymers [24–26]. Therefore, the pressing technique was used in both SLS and IM PA-12, PLA and PETG, while in the resin the blade sliding technique (razor sliding) was used due to the rapid crack growth. Blades with thicknesses of 0.3 mm and tip radii of 5.3 μm were used for both the pressing and razor sliding techniques. These blades are commonly employed in ultramicrotomes, to guarantee sharp cracks with tip radius smaller than 20 μm [27]. The procedure for pressing has been the positioning of the blade on a previously marked location and its introduction at low speed in the specimen, while in the sliding procedure the blade was positioned on the marked point in the specimen and slid until obtaining the estimated crack size. The cracks introduced had nominal lengths of 0.2, 0.3, 0.5, 1, 2, 2.5 and 3 mm, with 3 specimens per condition and material. The crack front of all the specimens was inspected via optical microscopy prior to testing to ensure no visual damage produced during crack introduction. Those which presented damage were automatically discarded. The final crack measurement was conducted in accordance with the methodology delineated in the ISO 13586 standard [28]. In this procedure, the mean of five crack length measurements is calculated, taken at the edges, at the centre and at equidistant points to them. To ensure accuracy, the mean is calculated ensuring that none of the measurements differ by more than 10 % from the mean obtained. To achieve this objective, a Zeiss Stemi 305 Stereo Microscope, equipped with a Zeiss Axiocam 208 digital camera and ZEN image acquisition and processing software, was employed. In cases where the optical conditions were inadequate for precise determination of crack length, Scanning Electron Microscopy was employed on a Hitachi S-3400 N. To this end, the sample was coated with a conductive layer in an Emitech K550X sputter coater for 45 s at a current of 25 mA, and images were obtained at an accelerating voltage of 10 keV.

From the specimens with the longest cracks, that is, nominal initial crack lengths of 3 mm, the critical stress intensity factor or fracture toughness K_{IC} was also obtained for PLA, PET-G and the thermosetting resin Monocure following the guidelines reported by Zhu [29]. These cracked samples resemble the Single Edge Notch Tension (SENT) configuration with an initial crack length, a_0, to width, W, ratio of 0.4. If the requirements of LEFM approach were verified, the fracture toughness was computed from:

Table 2

Average roughness through the profile R_a and the average of the maximum peak to valley distances, R_z, for the MONOCURE 3D, PLA, PET-G, SLS PA-12 at 0° and 90° orientations and IM PA-12.

Material	R_a (μm)	R_z (μm)
MONOCURE 3D	2 ± 0.4	12 ± 2
PLA	4 ± 0.4	26 ± 8
PET-G	3.3 ± 0.5	56 ± 4
PA-12 SLS 0°	12 ± 1	69 ± 8
PA-12 SLS 90°	12 ± 4	60 ± 20
PA-12 IM	0.4 ± 0.2	3 ± 2

$$K_{IC} = \frac{P}{BW}\sqrt{\pi a}f\left(\frac{a}{W}\right) \tag{4}$$

where B is the thickness, W the width, P the maximum load and f(a/W) is the geometric factor given by [29,30]:

$$f\left(\frac{a}{W}\right) = 0.2832 + 3.8497\left(\frac{a}{W}\right) - 1.4885\left(\frac{a}{W}\right)^2 + 4.1716\left(\frac{a}{W}\right)^3 + 9.9094\left(\frac{a}{W}\right)^4 - 7.4188\left(\frac{a}{W}\right)^5 \tag{5}$$

In case non-linearity is dominant, the J-integral at crack growth initiation, J_{IC}, was determined through:

$$J_{IC} = \frac{\eta U}{B(W-a)} \tag{6}$$

With U the area under the load displacement curve at crack growth initiation and η the adimensional factor based on numerical results [30,31]:

$$\eta = 1.067 - 1.767\left(\frac{a}{W}\right) + 7.808\left(\frac{a}{W}\right)^2 - 18.269\left(\frac{a}{W}\right)^3 + 15.295\left(\frac{a}{W}\right)^4 - 3.083\left(\frac{a}{W}\right)^5 \tag{7}$$

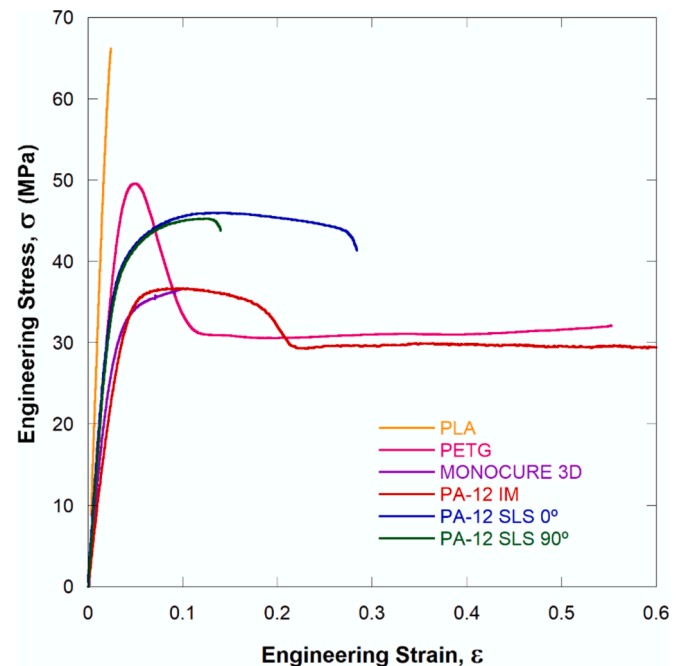The critical stress intensity factor is obtained from J-integral through the

Fig. 4. Engineering stress – engineering strain curves obtained from specimens with no cracks.

Table 3
Young Modulus, E, Tensile strength, σ_T, elongation at maximum stress, ε_u, and elongation at break, ε_R, of MONOCURE 3D, PLA, PET-G, PA-12 SLS and PA-12 IM obtained from the tensile tests of plain specimens.

Material	E (GPa)	σ_T (MPa)	ε_u (%)	ε_R (%)
MONOCURE 3D	1.0 ± 0.3	36 ± 1	8 ± 2	8 ± 2
PLA	3.1 ± 0.1	65 ± 1.5	2.0 ± 0.5	2.0 ± 0.5
PET-G	1.7 ± 0.2	48 ± 1	4.4 ± 0.5	200*
PA-12 SLS 0°	1.64 ± 0.03	47 ± 1	13.1 ± 0.6	27 ± 2
PA-12 SLS 90°	1.58 ± 0.04	44 ± 2	9 ± 3	10 ± 4
PA-12 IM	1.34 ± 0.04	41 ± 1	11 ± 5	64 ± 4

*Tests stopped when the deformations reached 200 % of engineering strain.

expression:

$$K_J = \sqrt{E^* J_{IC}} \tag{8}$$

With $E^* = E$ for plane stress and $E^* = \frac{E}{1-\nu^2}$ for plane strain where E is the Young's modulus of the material and ν is the Poisson's ratio.

In case of SLS PA-12 0°, SLS PA-12 90° and IM PA-12, standardized tests following the ASTM E1820 standard were carried out in Compact Tension (CT) specimens by the authors. The methodology, results and analysis are already published in [20–22].

3. Results

3.1. Surface roughness measurements in plain specimens

Table 2 shows the surface roughness measurements obtained in plain specimens. The smallest surface defect size is obtained in the specimens of PA-12 manufactured by IM, being the following value obtained in the MONOCURE 3D resin and the highest roughness obtained in both orientations of the PA-12 manufactured by SLS, while PLA and PET-G, both manufactured by FDM have shown intermediate values. From now on, the surface defect size of the plain samples was considered as R_z.

3.2. Tensile properties in plain specimens

Fig. 4 shows representative engineering stress, σ, vs engineering strain, ε, curves obtained from tensile tests of the materials under study with no cracks. The dissimilarity in the mechanical response is obvious. PLA showed the highest mechanical strength but also the most brittle, and as expected the MONOCURE resin presented the lowest mechanical strength along with the IM PA-12, but the latter displayed great ductility. This is more easily explained in numbers, looking at the average values of the Young Modulus (E), the tensile strength (σ_T), the elongation at maximum stress (ε_u), and the elongation at break (ε_R) collected in Table 3 together with the standard deviation.

As mentioned, the highest value of the mechanical tensile strength was obtained for PLA, followed by PET-G, SLS PA-12 0° and 90°, IM PA-12, and the lowest for the thermoset MONOCURE 3D. As for the elongation at break, the highest value was obtained for PET-G, reaching deformations of 200 %. The next values, in descending order and quite far from it, are those of PA-12 IM, PA-12 SLS 0° and 90°, MONOCURE 3D and finally PLA. As expected, the thermoset presented brittle behaviour and among the thermoplastics, the PLA was clearly the most brittle with the highest tensile strength at the expense of the elongation at break while the more ductile was PET-G. Regarding the load bearing capacity, PET-G and PA12 presented similar values. Regarding the effect of the processing technique in PA12, IM specimens were more ductile than SLS samples and within the latter, more brittle behaviour was obtained when the layered structure was perpendicular to the applied load direction [20–22].

3.3. Mechanical performance of cracked samples

Fig. 5.a, 5.b, 5.c, 5.d and 5.e display the representative load–displacement records obtained from tensile tests performed on plain specimens and on specimens with cracks of different lengths for MONOCURE 3D resin, PLA, PET-G, PA-12 SLS 0° and PA-12 IM, respectively. In all cases, the displacement recorded by the contact extensometer is shown, except in PA-12 IM, where, due to the high deformability, the displacement was well beyond the limit of the contact extensometer and therefore it was decided to show the displacement recorded by the load train. The only curves missing are those of PA-12 SLS 90°. SLS specimens presented in general a large number of defects (pores, unmolten particles, etc) especially located between layers. The influence of these defects was most detrimental when the load was applied perpendicularly to the layer deposition, that is, at 90° orientation. That is the reason why in PA-12 SLS 90°, the failure occurred mostly in zones other than where the crack was introduced, to the point that the number of failed tests was such that it prevented the strength diagrams from being obtained. Stiffness variations observed in the figures are due to small dimensional variations between the tested specimens caused by the additive manufacturing techniques used. In all of them, the load at failure decreases as the crack size increases, also reaching a smaller displacement. Specifically, while in the MONOCURE 3D material (Fig. 5.a) it is observed that the presence of cracks greatly affects its resistance capacity, the rest of the materials undergo a more gradual drop. Furthermore, although in PLA (Fig. 5.b) the presence of cracks also affects the load bearing capacity from the shortest crack, in the case of PET-G (Fig. 5.c), PA-12 SLS 0° (Fig. 5.d) and PA-12 IM (Fig. 5.e) the load bearing capacity hardly decreases with cracks smaller than 0.7 mm for PA-12 SLS 0° and 1 mm for PA-12 IM and PET-G, producing only a decrease in ductility.

As can be seen in the previous graphs, the crack lengths indicated are not the nominal values mentioned in the methodology section, but the real dimensions measured on the fracture surfaces. Fig. 6 illustrates the fracture surfaces of the materials under study, where the initial crack length introduced by razor sliding is pointed out by an arrow and delineated by a white dashed line. Furthermore, the transition zone between the initial crack and its subsequent propagation is visible in the lower left-hand corner of each image.

4. Discussion

The experimental results obtained can be combined in a residual strength diagram, which represents the maximum strength versus crack length (Fig. 1). Firstly, in order to locate the corresponding points on the specimens without cracks, the surface roughness (Rz from Table 2) has been chosen as the initial characteristic flaw size. In addition, the results of fracture tests carried out by the same authors in PA-12 IM, PA-12 SLS 0° and PA-12 SLS 90° using the Compact Tension (CT) configuration and already available in the literature, have been also included [20–22], as well as the fracture toughness obtained from the specimens with the longest crack lengths following the methodology reported by Zhu [29] in PLA, PET-G and Monocure 3D.

Regarding the fracture toughness obtained from the fracture tests, the values of PLA are in the range of those reported by Ahmed and Susmel [32,33], Cicero et al. [34], Marşavina et al. [35] and Ramirez et al. [36] when the building orientation was 0° and similar printing speeds. Regarding PET-G, the values obtained are similar to those obtained by Karger-Kocsis et al. [37] and Choi et al. [38] in extruded sheets but half the values of those determined by Martínez et al. [24] in a commercial grade. And the thermosetting resin presented values typical of these brittle materials [12]. Concerning PA-12 processed via SLS and IM, the fracture values are in accordance with those found in the literature [20–22].

Fig. 7 shows these diagrams for all the materials under study and testing conditions, including the fit of the experimental data to equation
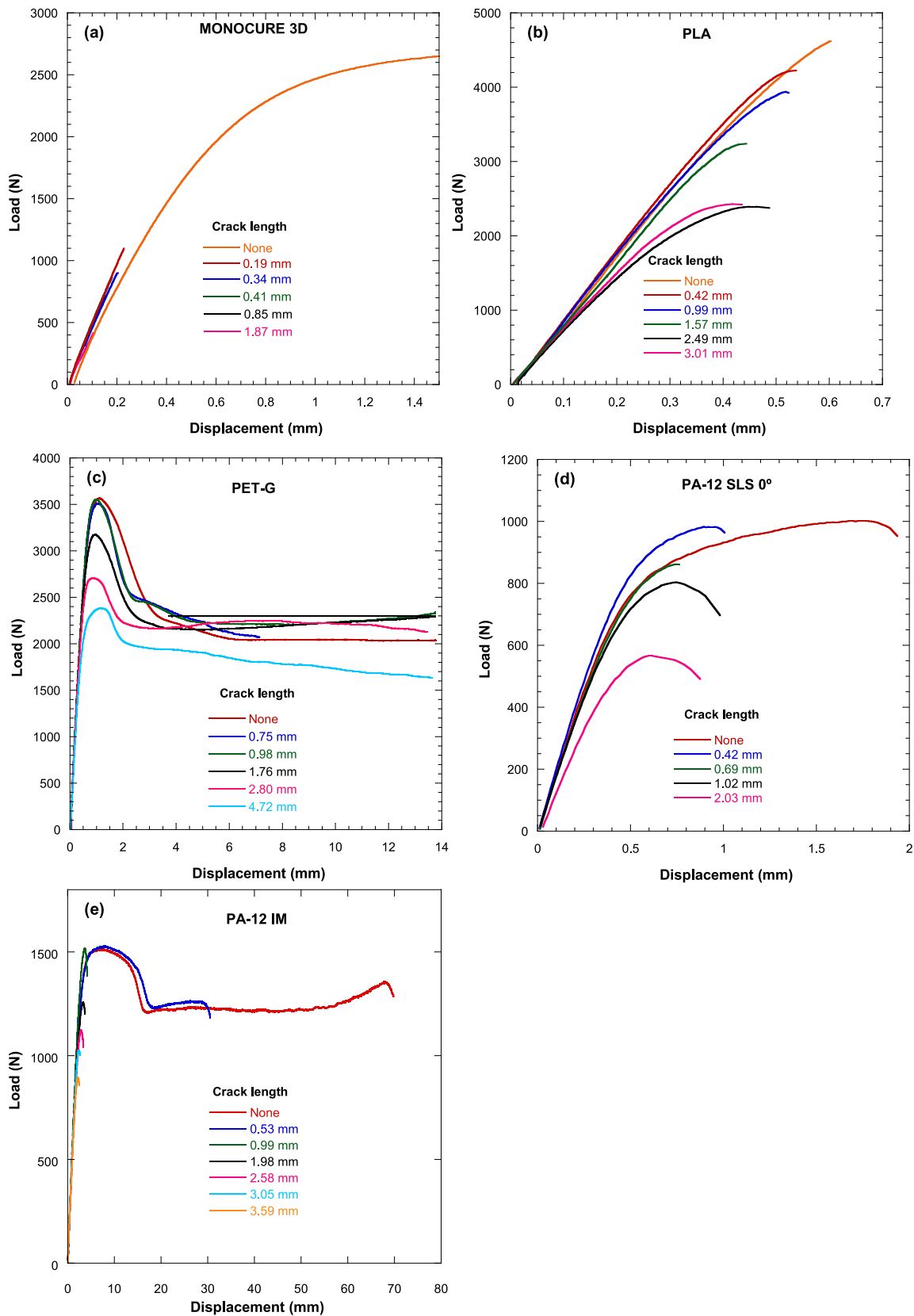
Fig. 5. Force-displacement records obtained in tensile tests carried out on smooth specimens and with cracks of different lengths in (a) MONOCURE 3D, (b) PLA, (c) PET-G, (d) PA-12 SLS 0° and (e) PA-12 IM.
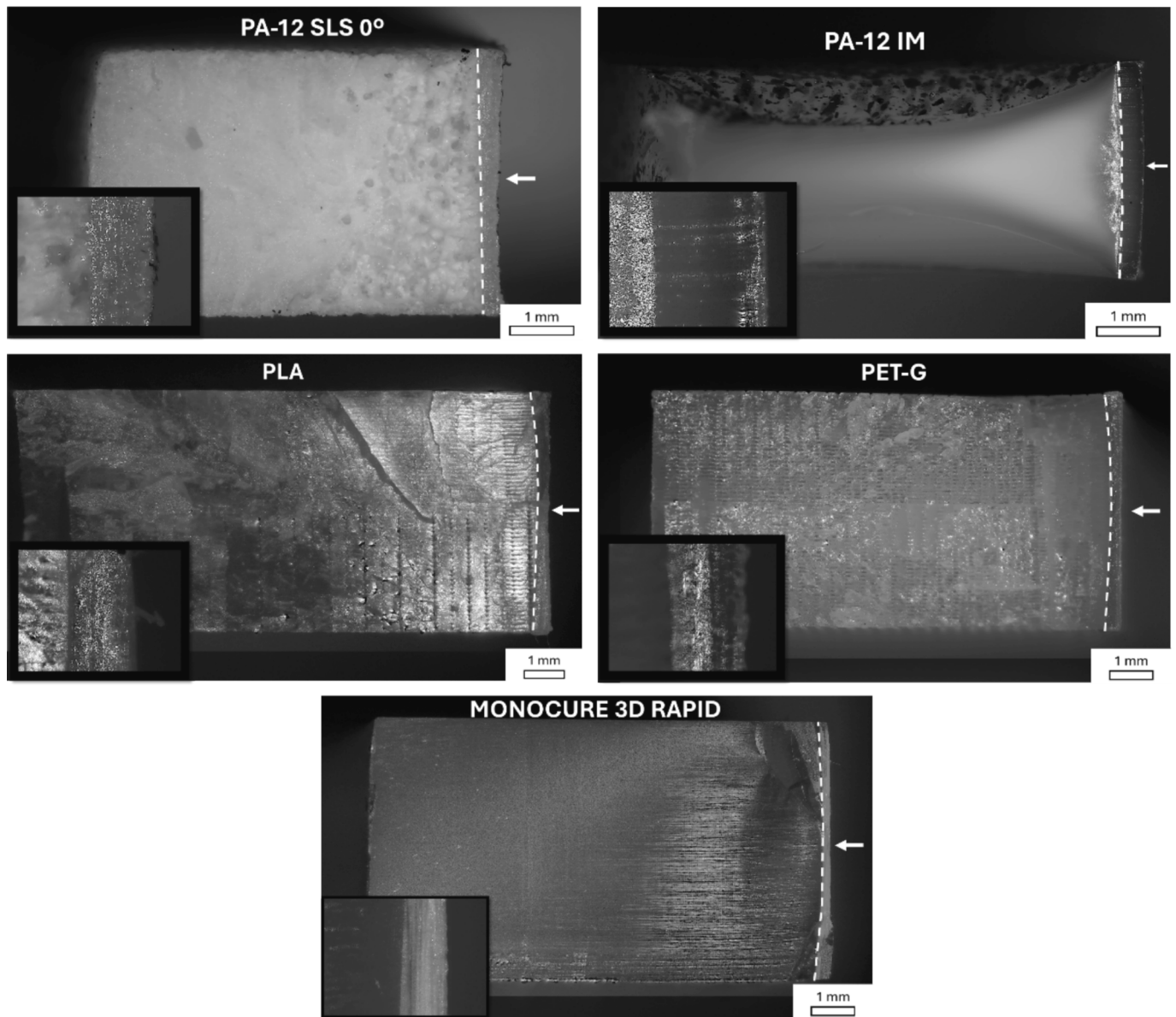
Fig. 6. Fracture surfaces of cracked specimens with initial crack lengths between 0.2 and 0.4 mm in PA-12 SLS 0°, PA-12 IM, PET-G, PLA and MONOCURE 3D RAPID. The white arrow indicates the zone of introduction of the initial crack.

(2). The results of the fitting provide the values of σ_T and l_0 shown in Table 4. Following the theory of the critical distances [11], these two material constants, σ_T and l_0, can be combined to estimate the fracture toughness, K_c^*, through the relationship:

$$K_c^* = \sigma_T \sqrt{\pi l_0} \qquad (9)$$

The comparison of the estimated fracture toughness values K_c^* with those measured experimentally K_{IC} is quite acceptable in all cases, indicating that the theory of critical distances can be a consistent first approximation to determine the fracture toughness of these additive manufactured polymers and its ability to tolerate the presence of defects.

The values of tensile strength obtained from plain samples (Table 3) and the fracture stress resulting from the fitting of the experimental values to equation (2) (Table 4) are rather similar. This indicates that the approach (equation (2)) reproduces adequately the behaviour in the regions of microstructurally short and long cracks, but also provides information in the region of physically short cracks where the characterization methods are poorly defined.

Throughout this description, the characteristic length l_0 plays a leading role. As can be seen in Table 4, materials of imminent brittleness such as resins have values of l_0 of the order of microns, being therefore very sensitive to the presence of defects. In contrast, more ductile thermoplastics such as PET-G have much greater capacity to withstand the presence of defects without reducing their strength, which is manifested in substantially higher l_0 values.

Thus, the most obvious physical interpretation is related to the size of the defect that produces a significant decrease in the load bearing capacity of the component. Although attempts have been made on numerous occasions to relate l_0 with microstructural characteristics, success has been relative since it seems that other factors, including geometry, can affect it. In particular, numerous authors have endeavoured to ascribe a tangible physical significance to the characteristic lengths, particularly in the context of metals. In cases where the values of l_0 are relatively small, several authors have established a correlation between them and microstructural characteristics. El Haddad linked them with the crystallographic grain size in steels and titanium alloys [7], while Ciavarella, also in steels, associated them with the distance from the surface to the first microstructural barrier that a crack could
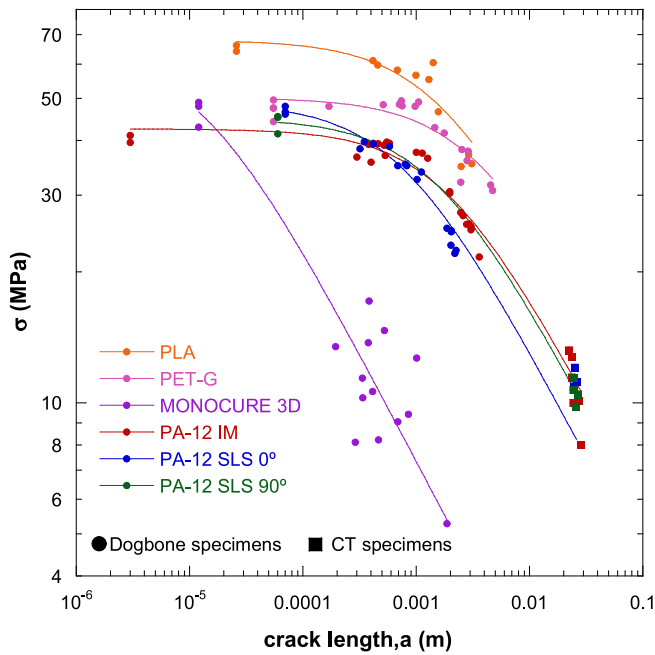
Fig. 7. Residual strength diagram of MONOCURE 3D resin, and thermoplastic polymers PLA, PETG, PA-12 SLS 0°, PA-12 SLS 90° and PA-12 IM.

Table 4

Fracture stress, σ_T, characteristic length, l_0, obtained from the fitting of the experimental data displayed in Fig. 4 to equation (1), fracture toughness computed following the theory of the critical distances (equation (9)), K_c^*, [11] and K_{IC} values obtained from experimental fracture tests [20–22].

Material	σ_T (MPa)	l_0 (mm)	K_c^* (MPa$\sqrt{m}$)	K_{IC} (MPa$\sqrt{m}$)
MONOCURE 3D	42 ± 3	0.032 ± 0.008	0.4 ± 0.1	0.50 ± 0.03
PLA	68 ± 3	1.6 ± 0.4	4.8 ± 1.2	4.8 ± 0.5
PETG	50 ± 1	3.5 ± 0.7	5.2 ± 0.9	5.6 ± 1.5
SLS PA-12 0°	49 ± 1	0.75 ± 0.08	2.4 ± 0.2	3.2 ± 0.2
SLS PA-12 90°	45 ± 1	1.1 ± 0.2	2.6 ± 0.4	2.9 ± 0.2
IM PA-12	44 ± 2	1.4 ± 0.2	2.9 ± 0.4	3.1 ± 0.4

encounter [8]. In other instances, as in non-metallic materials (such as building materials, composites, or certain polymers) or in materials lacking a microstructure due to their amorphous nature, the characteristic length can be correlated with the size of the damage zone. In such cases, the characteristic length can span a range of only a few hundred microns to millimetres, often exceeding the scale of microstructural features by at least one order of magnitude. This is due to the multitude of factors involved in the formation and propagation of damage. In this case, in an attempt to associate the characteristic length with the most significant defects, microstructural and mesoscopic features that could influence the mechanical response of the materials examined, the authors do not provide a link between the size of microstructural features or the mesoscopic structures (Tables 1 and 2) and the characteristic lengths l_0 (Table 4) that have been obtained. It is important to highlight that the l_0 obtained in PLA is similar to the one reported by Ahmed and Susmel [33], ~2,4 mm, when evaluating the failure of notched 3D-printed PLA using the theory of critical distances. Ahmed and Susmel [33] also employed the static Kitagawa-Takahashi diagrams in quasi-static conditions to show the transition from the short to long crack regime applied to notches.

Another relationship that some authors have sought to ascribe to the characteristic length l_0 in polymeric materials is the estimation of the length of the zone affected by the emergence of crazes during fracture. This estimation is founded upon the strip-yield model proposed by Dugdale-Barenblatt and set forth in equation (10) [39,40]:

Table 5

Estimation of the craze zone lengths, l_0^{crazes}, obtained from equation (3) of the MONOCURE 3D resin, PLA, PET-G SLS PA-12 and IM PA-12 studied. For purposes of comparison, the characteristic lengths l_0 shown in Table 4 are also included.

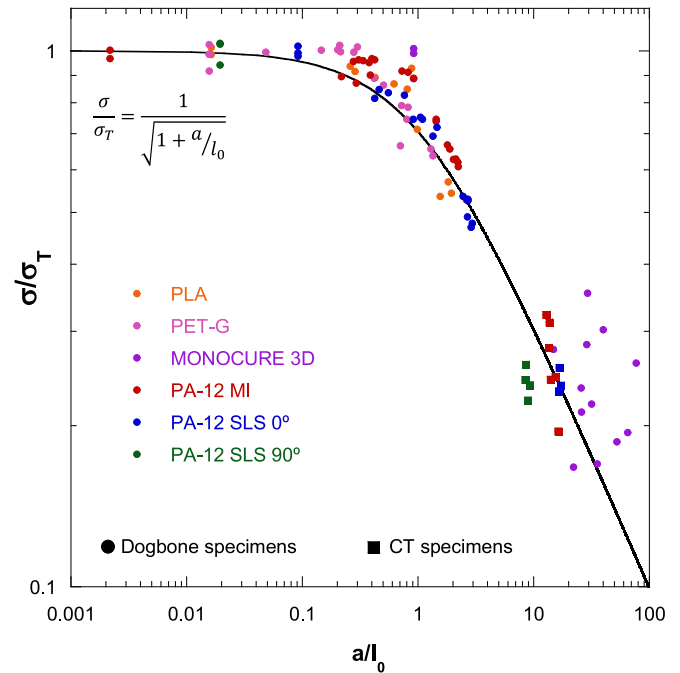| Material	l_0^{crazes} (mm)	l_0 (mm)
MONOCURE 3D	0.056 ± 0.001	0.032 ± 0.008
PLA	1.96 ± 0.3	1.6 ± 0.4
PET-G	5.10 ± 3.4	3.5 ± 0.7
SLS PA-12 0°	1.68 ± 0.2	0.75 ± 0.08
SLS PA-12 90°	1.63 ± 0.2	1.1 ± 0.2
IM PA-12	1.95 ± 0.46	1.4 ± 0.2

Fig. 8. Normalized residual strength diagram in which all the experimental data of the materials under study, MONOCURE 3D, PLA, PET-G, PA-12 SLS 0°, PA-12 SLS 90° and PA-12 IM, are included. Data obtained from fracture tests carried out on CT specimens are also plotted.

$$l_0^{crazes} = \frac{\pi}{8}\left(\frac{K_{IC}}{\sigma_T}\right)^2 \tag{10}$$

Applying this expression to the experimental data obtained in this study, the craze zone lengths, l_0^{crazes} are shown in Table 5. For purposes of comparison, the characteristic lengths obtained previously, l_0, are also included. Obviously, there is correlation between the values of l_0 and l_0^{crazes}, however, the Dugdale-Barenblatt model estimates a greater length of the affected zone, rendering it more conservative. Based on this conservative estimation, Williams et al. introduced a modification to equation (10), whereby the yield stress σ_T is substituted for the crazing stress, which is associated with the appearance of crazes [41]. Although the crazing stress has not been directly measured in this study, it can be observed that the incorporation of a crazing stress value, which is lower than the yield stress, results in an increment in the calculated l_0^{crazes}.

Finally, from the two material constants of the theory of critical distances shown in Table 4, the normalized residual resistance diagram has been obtained, representing the normalized stress at failure, σ/σ_T, against the normalized crack size, a/l_0. This diagram is shown in Fig. 8. It can be seen how the results of the different materials tested are grouped according to the relationship shown in equation (2).

5. Conclusions

This work has studied the structural integrity of thermosetting resin MONOCURE 3D and thermoplastic polymers PLA and PET-G manufactured by FDM and PA-12 manufactured by SLS and injection moulding through residual strength diagrams. The semi-empirical approach based on that of El Haddad has been used to analyse the behaviour in the regions of microstructurally short and long cracks and to provide information on the region of physically short cracks. The parameters resulting from the fitting of the experimental data obtained from specimens with different crack lengths are the same as the values of the parameters measured experimentally. Moreover, the value of the characteristic length has allowed to classify the different polymeric materials according to their sensitivity to the presence of defects.

CRediT authorship contribution statement

A.J. Cano: Writing – original draft, Methodology, Investigation, Funding acquisition. **A. Salazar:** Writing – review & editing, Supervision, Methodology, Investigation, Funding acquisition, Formal analysis, Conceptualization. **J. Rodríguez:** Writing – review & editing, Supervision, Methodology, Funding acquisition, Formal analysis, Conceptualization.

Declaration of competing interest

The authors declare that they have no known competing financial interests or personal relationships that could have appeared to influence the work reported in this paper.

Acknowledgments

Data availability

Data will be made available on request.

References

[1] M. Harold Jr, T. Troy, Air Force aircraft structural integrity program: Airplane requirements. Technical Report ASD-TR-66-57, Aeronautical Systems Division, Air Force Systems Command, Ohio, 1970.

[2] C. Feddersen, Evaluation and prediction of the residual strength of center cracked tension panels, in: Damage Toler. Aircr. Struct. ASTM STP 486, ASTM International, West Conshohocken, PA, 1971, pp. 50–78. Doi: 10.1520/STP26673S.

[3] R.A. Smith, Short fatigue cracks, Fatigue mechanics: advances in quantitative measurement of physical damage, ASTM STP, 1983.

[4] R.I. Stephens, A. Fatemi, R.R. Stephens, H.O. Fuchs, Metal Fatigue in Engineering, second ed., Wiley, New York, 2001.

[5] K.J. Miller, The short crack problem, Fatigue Fract. Eng. Mater. Struct. 5 (1982) 223–232, https://doi.org/10.1111/j.1460-2695.1982.tb01250.x.

[6] H. Kitagawa, S. Takahashi, Applicability of fracture mechanics to very small cracks or the cracks in the early stage. Proceedings of second international conference on mechanical behaviour of materials. Metals Park: American Society for Metals; 1976, pp. 627–631.

[7] M. El Haddad, T. Topper, K. Smith, Prediction of non-propagating cracks, Eng. Fract. Mech. 11 (1979) 573–584, https://doi.org/10.1016/0013-7944(79)90081-X.

[8] M. Ciavarella, F. Monno, On the possible generalizations of the Kitagawa-Takahashi diagram and of the El Haddad equation to finite life, Int. J. Fatigue 28 (12) (2006) 1826–1837, https://doi.org/10.1016/j.ijfatigue.2005.12.001.

[9] K. Sadananda, S. Sarkar, Modified Kitagawa diagram and transition from crack nucleation to crack propagation, Metall. Mater. Trans. A 44A (2013) 1175–1189, https://doi.org/10.1007/s11661-012-1416-x.

[10] J. Planas, M. Elices, G.V. Guinea, F.J. Gómez, D.A. Cendón, I. Arbilla, Generalizations and specializations of cohesive crack models, Eng. Fract. Mech. 70 (2003) 1759–1776, https://doi.org/10.1016/S0013-7944(03)00123-1.

[11] D. Taylor, The theory of critical distances. A new perspective in Fracture Mechanics, first ed., Elsevier, Oxford, 2007. Doi: 10.1016/B978-0-08-044478-9.X5000-5.

[12] J. Rodríguez, A. Salazar, F.J. Gómez, Y. Patel, J.G. Williams, Fracture of notched samples in epoxy resin: Experiments and cohesive model, Eng. Fract. Mech. 149 (2015) 402–411, https://doi.org/10.1016/j.engfracmech.2015.06.058.

[13] A. Serrano, M.A. Garrido, A. Salazar, J. Rodríguez, Understanding the failure of epoxy resin U-notched samples using cohesive models, Theor. Appl. Fract. Mech. 102 (2019) 46–50, https://doi.org/10.1016/j.tafmec.2019.04.002.

[14] D. Taylor, The theory of critical distances: a link to micromechanisms, Theor. Appl. Fract. Mech. 90 (2017) 228–233, https://doi.org/10.1016/j.tafmec.2017.05.018.

[15] S.-X. Wu, Y.-W. Mai, B. Cotterell, C. Wiet Le, Ductile-brittle fracture transition due to increasing crack length in a medium carbon steel, Acta Metall. Mater. 39 (1991) 2527–2532, https://doi.org/10.1016/0956-7151(91)90068-C.

[16] V.K. Sutrakar, B. Javvaji, P.R. Budarapu, Fracture strength and fracture toughness of graphene: MD simulations, Appl. Phys. A Mater. Sci. Process. 127 (2021) e949.

[17] J.P. Berry, Fracture processes in polymeric materials. II. The tensile strength of polystyrene, J. Polym. Sci. 50 (1961) 313–321, https://doi.org/10.1002/pol.1961.1205015405.

[18] 3D Hubs, Worldwide most used 3D printing materials, as of July 2018* [Graph], Statista, https://www.statista.com/statistics/800454/worldwide-most-used-3d-printing-materials/.

[19] J.R.C. Dizon, A.H. Espera, Q. Chen, R.C. Advincula, Mechanical characterization of 3D-printed polymers, Addit. Manuf. 20 (2017) 44–67, https://doi.org/10.1016/j.addma.2017.12.002.

[20] A.J. Cano, Fatigue behaviour of Polyamide 12 processed by Selective Laser Sintering, Universidad Rey Juan Carlos, 2021. PhD thesis.

[21] A.J. Cano, A. Salazar, J. Rodríguez, Effect of temperature on the fracture behavior of polyamide 12 and glass-filled polyamide 12 processed by selective laser sintering, Eng. Fract. Mech 203 (2018) 66–80, https://doi.org/10.1016/j.engfracmech.2018.07.035.

[22] A. Salazar, A.J. Cano, J. Rodríguez, Mechanical and fatigue behaviour of polyamide 12 processed via injection moulding and selective laser sintering. Analysis based on Kitagawa-Takahashi diagrams, Eng. Fract. Mech. 275 (2022) 108825, https://doi.org/10.1016/j.engfracmech.2022.108825.

[23] ASTM D638-14, Standard Test Method for Tensile Properties of Plastics. ASTM International. https://www.astm.org/d0638-14.html.

[24] A.B. Martínez, N. León, D. Arencón, J. Rodríguez, A. Salazar, On the effect of the different notching techniques on the fracture toughness of PETG, Polymer Test. 32 (7) (2013) 1244–1252, https://doi.org/10.1016/j.polymertesting.2013.07.016.

[25] A. Salazar, J. Rodríguez, A.B. Martínez, The role of notch sharpening on the J-fracture toughness of thermoplastic polymers, Eng. Fract. Mech. 101 (2013) 10–22, https://doi.org/10.1016/j.engfracmech.2012.07.006.

[26] A.B. Martínez, A. Salazar, N. León, S. Illescas, J. Rodríguez, Influence of the notch-sharpening technique on styrene-acrylonitrile fracture behaviour, J. Appl. Polym. Sci. 133 (2016) 43775, https://doi.org/10.1002/app.43775.

[27] G.E. Hale, F. Ramsteiner, J-Fracture Toughness of Polymers at Slow Speed, in: D.R. Moore, A. Pavan, J.G. Williams (Eds.), Fracture Mechanics Testing Methods for Polymers, Adhesives and Composites, ESIS Publication 28, Elsevier 2001, pp. 140–157.

[28] ISO 13586:2018. Plastics — Determination of fracture toughness (G_{IC} and K_{IC}) — Linear elastic fracture mechanics (LEFM) approach, 2018, International Organization for Standarization.

[29] X.K. Zhu, Progress in development of fracture toughness test methods for SENT specimens, Int. J. Pressure Vessels Pip. 156 (2017) 40–58, https://doi.org/10.1016/j.ijpvp.2017.07.004.

[30] S. Cravero, C. Ruggieri, Estimation procedure of J-Resistance curves for SE(T) fracture specimens using unloading compliance, Eng Fract Mech 74 (2007) 2735–2757, https://doi.org/10.1016/j.engfracmech.2007.01.012.

[31] L.L.S. Mathias, D.F.B. Sarzosa, C. Ruggieri, Effects of specimen geometry and loading mode on crack growth resistance curves of a high-strength pipeline girth weld, Int. J. Pressure Vessels Pip. 111–112 (2013) 106–119, https://doi.org/10.1016/j.ijpvp.2013.06.003.

[32] A.A. Ahmed, L. Susmel, A material length scalebased methodology to assess static strength of notched additively manufactured polylactide (PLA), Fatigue Fract. Eng. Mater. Struct. 41 (10) (2018) 2071–2098, https://doi.org/10.1111/ffe.12746.

[33] A.A. Ahmed, L. Susmel, Static assessment of plain/notched polylactide (PLA) 3D-printed with different in-fill levels: equivalent homogenised material concept and Theory of Critical Distances, Fatigue Fract. Eng. Mater. Struct. 42 (4) (2019) 883–904, https://doi.org/10.1111/ffe.12958.

[34] S. Cicero, V. Martínez-Mata, L. Castanon-Jano, A. Alonso-Estebanez, B. Arrojo, Analysis of notch effect in the fracture behaviour of additively manufactured PLA and graphene reinforced PLA, Theor. Appl. Fract. Mech. 114 (2021) 103032, https://doi.org/10.1016/j.tafmec.2021.103032.

[35] L. Marşavina, C. Valean, M. Marghitaş, E. Linul, N. Razavi, F. Berto, R. Brighenti, Effect of the manufacturing parameters on the tensile and fracture properties of FDM 3D-printed PLA specimens, Eng. Fract. Mech. 274 (2022) 108766, https://doi.org/10.1016/j.engfracmech.2022.108766.

[36] C. Ramirez, E. Agaliotis, V. Pettarin, Fracture toughness and overall characterization of PLA based biocomposites with natural fibers: a comparative study, Polymer 307 (2024) 127309, https://doi.org/10.1016/j.polymer.2024.127309.

[37] J. Karger-Kocsis, T. Bárány, E.J. Moskala, Plane stress fracture toughness of physically aged plasticized PETG as assessed by the essential work of fracture (EWF) method, Polymer 44 (2003) 5691–5699, https://doi.org/10.1016/S0032-3861(03)00590-1.

[38] M.S. Choi, J.H. Lee, B.H. Choi, Mechanical and fracture properties of poly(ethylene terephthalate) with glycol/carbon nanotube nanocomposite films under accelerated weathering conditions, J. Mech. Sci. Technol. 35 (9) (2021) 3837–3845. http://doi.org/10.1007/s12206-021-2107-6.

[39] D.S. Dugdale, Yielding in steel sheets containing slits, J. Mech. Phys. Solids 8 (1960) 100–104, https://doi.org/10.1016/0022-5096(60)90013-2.

[40] G.I. Barenblatt, The mathematical theory of equilibrium cracks in brittle fracture, Adv. Appl. Mech. 7 (1962) 55–129.

[41] J.G. Williams, G.P. Marshall, Environmental crack and craze growth phenomena in polymers, Proc. R. Soc. London Ser. A-Math. Phys. Sci. 342 (1628) (1975) 55-77. https://www.jstor.org/stable/78617.